



## Distributed and localized faulting in extensional settings: Insight from the North Ethiopian Rift–Afar transition area

Roger Soliva<sup>1</sup> and Richard A. Schultz<sup>2</sup>

Received 4 May 2007; revised 6 November 2007; accepted 5 December 2007; published 19 March 2008.

[1] Extensional fault systems in the Earth's crust can exhibit two end-member geometries that we identify as distributed and localized faulting regimes. A satellite image analysis of fault populations from the Main Ethiopian Rift-Afar area reveals that the rift architecture contains these two faulting regimes. The occurrence of these regimes reveals a jump in the scale of fault segmentation and linkage. Strain localization at rift border zones exhibits particularly large-scale fault linkage and a power law size distribution. This regime replaces prior distributed fault systems, showing small-scale fault linkage and an exponential size distribution. The distributed faulting is interpreted as confined to the thick trap basalt carapace. We show that continental fault systems can develop by a combination of these two geometries, and we demonstrate how to quantitatively decipher the jump between them. **Citation:** Soliva, R., and R. A. Schultz (2008), Distributed and localized faulting in extensional settings: Insight from the North Ethiopian Rift–Afar transition area, *Tectonics*, 27, TC2003, doi:10.1029/2007TC002148.

### 1. Introduction

[2] In recent decades, quantitative analyses of fault populations in the Earth's crust have been mainly designed (1) to evaluate theories of fault growth [Walsh and Watterson, 1987; Lin and Parmentier, 1988; Cowie and Scholz, 1992; Cowie and Shipton, 1998; Schultz and Fossen, 2002] and (2) to predict fault geometries [Pickering et al., 1997; Maerten et al., 2002; Walsh et al., 2003; Soliva and Benedicto, 2004], which find applications in seismic hazard assessment and prediction, oil and gas exploration, hydrogeology, and waste storage. Other studies have aimed (3) to constrain geometrical terms in brittle strain analytical solutions [Scholz and Cowie, 1990; Schultz, 2003] and (4) to understand rift geometry [e.g., Gupta and Scholz, 2000a]. However, very few fault system analyses focused on evaluating distribution and localization of faulting, despite its importance in the understanding of extensional fault system

formation, seismicity localization, and the process of continental rifting.

[3] We define “distributed faulting” as fault systems composed of multiple fully overlapping and regularly spaced faults of small relative displacement [Cowie et al., 1994; Ackermann et al., 2001; Soliva et al., 2006]. In contrast, we define “localized faulting” as fault systems composed of interacting and linked faults that lead to the formation of a few very large faults accommodating a large proportion of the cumulative fault system strain [e.g., Scholz and Cowie, 1990; Cowie et al., 1995; Cladouhos and Marrett, 1996].

[4] Analyses of the spatial distribution of faulting in extensional settings have been emphasized and discussed using numerical or analogue modeling of the lithosphere [e.g., Buck, 1991; Hopper and Buck, 1996; Brun, 1999; Corti et al., 2003]. At this scale of deformation (e.g., Basin and Range province versus Main Ethiopian Rift (MER)), strain distribution is assumed to depend on a set of factors that affect the stability of the lithosphere, including strain rate [e.g., England, 1983], changes in buoyancy forces [e.g., Buck, 1991] and initial weakness [e.g., Fletcher and Hallet, 1983]. In these studies, extension of the brittle crust is the result of the lithospheric strength envelope's stability, and fault populations implicitly form as a result. However, changes in the geometry and other characteristics of the fault populations, paralleling similar observations made at smaller (e.g., outcrop) scales, suggest that distributed and localized faulting can affect, and not just be the result of, extension of the lithosphere [e.g., Handy, 1989].

[5] Normal fault systems commonly show a large component of strain localized on a few large coalesced faults [Walsh et al., 1991; Cladouhos and Marrett, 1996; Cowie and Shipton, 1998], that we define in this paper as “localized faulting,” the first end-member regime of fault system growth (Figure 1a). Since the beginning of statistical analysis of fault populations [e.g., Villemin and Sunwoo, 1987], this style of faulting has generally been assumed to be fractal, i.e., fragmented and having self-similar geometrical attributes. Fault system analysis revealed that fault size distribution, displacement length relation ( $D_{\max}$ - $L$ ), spacing ( $S$ ), overlap ( $O_v$ ) and connectivity are interdependent parameters and frequently self similar [e.g., Scholz and Cowie, 1990; Dawers et al., 1993; Cowie et al., 1995; Schlische et al., 1996; Cladouhos and Marrett, 1996; Cowie and Shipton, 1998].

[6] During the period of application of fractal analyses in the Earth sciences, a few studies revealed the existence of scale-dependent behavior [Cowie et al., 1994; Knott et al., 1996], which usually corresponds to fault systems showing

<sup>1</sup>Laboratoire Géosciences Montpellier, Université Montpellier II, Montpellier, France.

<sup>2</sup>Geomechanics–Rock Fracture Group, Department of Geological Sciences and Engineering, University of Nevada, Reno, Nevada, USA.

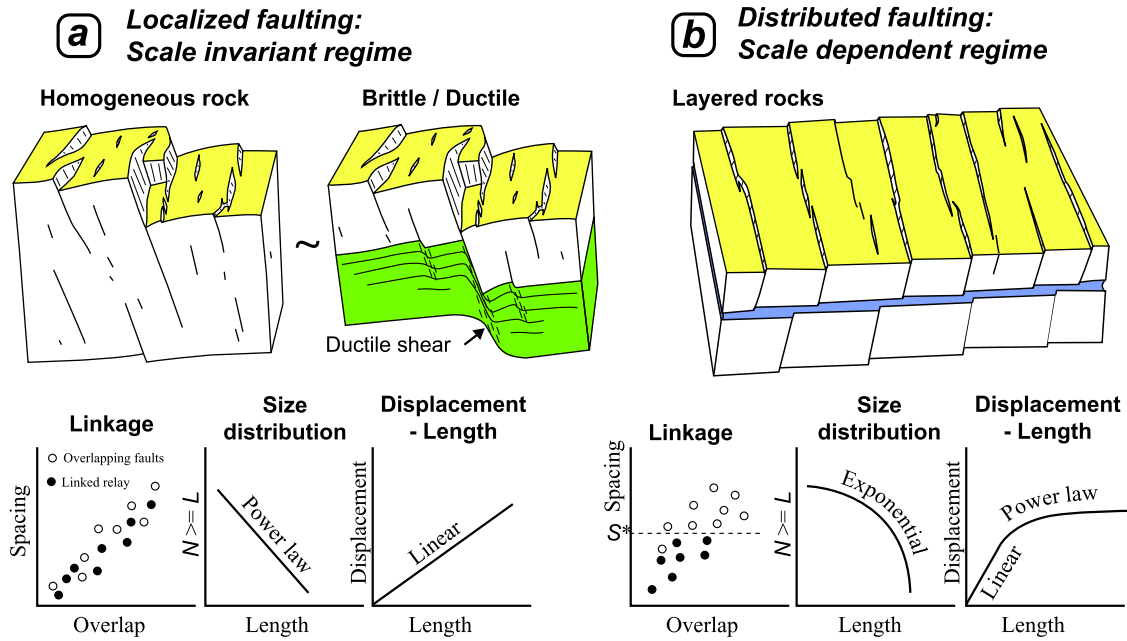


**Figure 1.** Localized versus distributed regimes in normal fault systems. (a) Summary of 3-D observations and empirical relations measured at the Earth’s surface. The fault system is defined as scale-invariant. (b) Summary of 3-D observations and empirical relations measured at the Earth’s surface. The fault system is defined as scale-dependent (dependent on brittle layer thicknesses). See section 2 for a detailed explanation and discussion.

distributed strain along nearly regularly spaced faults within a brittle mechanical unit [Gross *et al.*, 1997] (Figure 1b). Recent works focused on field observations [Soliva, 2004] and theory [Schultz and Fossen, 2002; Ackermann *et al.*, 2001] converge on the common existence of this second end-member case of faulting, that we define as “distributed faulting,” where all the fault system attributes (size distribution, displacement length relation, spacing, overlap and connectivity) are dependent on the brittle rock layer thickness containing the faults. This second end-member case is however rarely discussed [e.g., Schultz, 1999; Kim and Sanderson, 2005], and very few intermediate cases between these end-member faulting regimes have been described. As a result, the spatiotemporal interaction of these two faulting regimes remains largely undocumented despite its importance in understanding long-term seismicity, the evolution of continental rifting, or calculation of brittle strain. The MER-Afar transition area provides an example that records the interaction between these two regimes.

[7] The scaling properties of the fault populations from the MER–Afar transition were previously analyzed from the topography of the fault scarps [Gupta and Scholz, 2000a; Manighetti *et al.*, 2001]. Because of the young age of the faults and the arid climate of the region, the fault scarps are reasonably well preserved; however, the magnitudes of fault displacements may be unreliable because of differential accommodation by sediment infill and volcanic flows observed in this region [e.g., Taieb, 1975; Varet and Gasse, 1978; Audin *et al.*, 2001]. The scaling properties of the studied area were previously also analyzed and dis-

cussed without particular emphasis on the differences between rift segments and fault system parts of the area [Gupta and Scholz, 2000a; Manighetti *et al.*, 2001].

[8] In this paper, we first review field data and theories of fault growth consistent with the two end-member faulting regimes mentioned above. Next, we describe a transient intermediate case between these two end-members faulting regimes by providing a detailed analysis of the different structures (rift segments, border zone, plateau area) composing the Main Ethiopian Rift–Afar transition area. Analysis of the geometrical attributes of the faults reveals that the rift architecture is composed of (1) wide zones around rift segments showing a distributed faulting regime and (2) rift border zones characterized by the geometrical attributes of the localized regime. We discuss the coexistence and the spatiotemporal interaction of these fault growth regimes in terms of mechanical layering of the lithosphere and extension rates.

## 2. Review of Localized and Distributed Faulting in Extensional Settings

### 2.1. Localized Faulting

[9] When a fault system grows, the increase of fault size (1) increases the volume of reduced stress that shadows the activity of small faults, and (2) allows formation of large faults by coalescence, which promotes a fractal geometry of the fault population [Main *et al.*, 1990; Sornette *et al.*, 1990; Cladouhos and Marrett, 1996] (Figure 2a). The fault

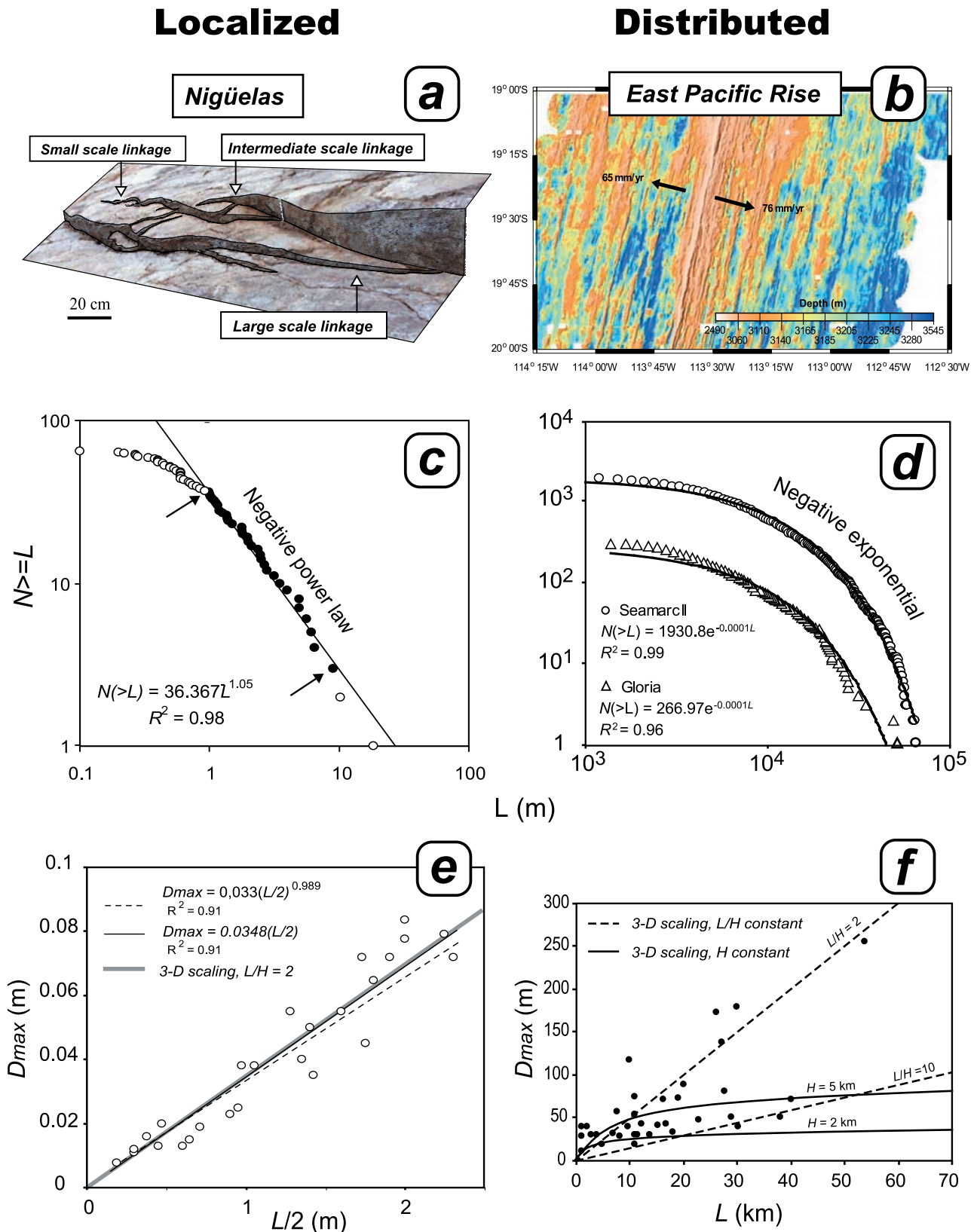


Figure 2

population grows in a scale-invariant and self-organized manner and results in a power law fault size distribution [e.g., *Scholz and Cowie*, 1990; *Schlische et al.*, 1996] (Figure 2c). This power law distribution mainly reflects strain localized along few large faults up to  $\sim 50\%$  for a case of power law exponent  $c = 2$  [*Kakimi*, 1980; *Villemin and Sunwoo*, 1987; *Scholz and Cowie*, 1990], with strain distributed on relatively small faults in a complementary proportion [*Walsh et al.*, 1991].

[10] Also observed along these examples, and very important for the aim of the present study, is a self-similar geometry of the fault segmentation (i.e., spacing, overlap, and displacement at relay zones) [*Peacock*, 2003; *Soliva and Benedicto*, 2004]. This scale-invariant process of linkage allows the formation of very large faults by linkage of smaller growing segments and therefore enhances the development of power law size distribution [e.g., *Cowie et al.*, 1995]. Figures 1a and 2a summarize this process by self-similar morphologies of linked and non linked segments present at various scales of a fault system. To understand this, *Gupta and Scholz* [2000b] showed that interaction and subsequent linkage develop preferentially for similar spacing/overlap ratios independent of the scale of observation. This therefore suggests that a self-similar segmentation geometry is mechanically possible in a fault population if the shear stress perturbation around the faults scales linearly with their length. A self-similar distribution of the stress reduction around faults is predicted where fault geometry and especially displacement-length scaling are on average scale-invariant.

[11] In this localized regime, fault displacements provide an important constraint. The displacement distribution of isolated faults entirely contained in homogeneous rocks has been documented as nearly linear between the fault tip and  $D_{\max}$ . A linear  $D_{\max}$ - $L$  scaling for fault populations has been also found for the same conditions [e.g., *Cowie and Scholz*, 1992; *Clark and Cox*, 1996; *Soliva*, 2004]. These attributes can be explained by three-dimensional (3-D) scaling post-yield fracture mechanics (PYFM) [see *Cowie and Scholz*, 1992; *Schultz and Fossen*, 2002] conditions with a constant, self-similar, aspect ratio  $L/H = 2$  [*Soliva et al.*, 2005] (Figure 2e). For these examples of growth in homogeneous rock, the displacement-length ratio of isolated faults is self similar (probably associated with radial fault propagation) and fault size distribution as well as the geometry of fault segmentation are scale-invariant. All these attributes are mechanically consistent and promote faulting in this first end-member regime.

## 2.2. Distributed Faulting

[12] The second end-member case concerns normal fault populations growing confined within a brittle layer of finite thickness. This scenario, analyzed by *Soliva et al.* [2006] for mesoscale fault systems, is characterized by faults growing with their vertical extent being limited, or restricted, by layers acting as mechanical barriers. This process leads to faults that grow in length with constant fault height and to a horizontally distributed fault system. Such vertically restricted faults are inferred from field observations as long segmented fault scarps of approximately constant height [also see *Nicol et al.*, 1996; *Koledoye et al.*, 2000]. In this regime, presented in Figures 1b and 2b, 2d, and 2f, isolated faults are no longer self similar in length and displacement distribution since they are vertically restricted, generally exhibiting flat topped displacement profiles [*Ackermann et al.*, 2001; *Soliva et al.*, 2005, 2006].

[13] The good correspondence between field observations and numerical modeling shows that regular fault spacing is due to the limited extent of the shear stress drop zone around the faults that is, in turn, a function of the short and constant fault height in the fault system [*Soliva et al.*, 2006]. This effect also limits the maximum distance for strong fault interaction, therefore controlling the dimensions of relay ramps and eventual fault linkage. This behavior (not restricted to a particular fracture mode) is not consistent with self-similar fault segmentation, but instead is related in a scale-dependent manner to the thickness of the brittle layer in which the faults are confined (see *Schultz and Fossen* [2002] for deformation bands and *Hu and Evans* [1989], *Rives et al.* [1992], and *Bai and Pollard* [2000] for joints). This “scale-dependent distributed regime” is therefore non-fractal and is characterized instead by a negative exponential size distribution (Figure 2d) when it is observed in the antiplane (horizontal for normal faults) dimension (Figure 2b). This exponential size distribution, which differs from the power law size scaling observed in nonrestricted fault systems (Figure 1), shows a smaller proportion of small faults and especially the absence of very large through-going faults that accumulate high strain compared to power law distributions (scale-invariant localized regime). Fault interaction and linkage are limited to specific (maximum) extent of stresses around the faults which is not linearly related to fault length, but instead is a function of the layer thickness [*Soliva et al.*, 2006]. The spatially limited fault interaction [e.g., *Willemsse*, 1997] inhibits the formation of very large faults and therefore the development of a power law size distribution [*Ackermann et al.*, 2001].

**Figure 2.** (left) Localized versus (right) distributed faulting in extensional fault systems at Nigüelas and at the East Pacific Rise. (a) Geometry of fault segmentation in the Nigüelas fault system (Betic cordillera, Spain), modified from *Soliva and Benedicto* [2004]. (b) Overview of the bathymetry at the East Pacific Rise showing normal faults cutting the brittle young oceanic crust. (c, d)  $D_{\max}$ - $L$  diagrams with 3-D scaling law fits calculated from the solution of *Schultz and Fossen* [2002] for constant fault height (solid lines) and constant fault aspect ratios (dashed lines). Height and aspect ratios are labeled on graphs. (e, f) Size distributions, which are best explained by negative exponential functions. Equations are labeled. Note the similarities between the two fault systems growing confined to brittle carbonate layers at Fumanyá and to the brittle oceanic crust at the EPR.

[14] The  $D_{\max}$ - $L$  scaling of these fault systems [Cowie *et al.*, 1994; Carbotte and Macdonald, 1994; dePolo, 1998; Poulimenos, 2000; Manighetti *et al.*, 2001; Bohnenstiehl and Carbotte, 2001; Polit *et al.*, 2005] is well explained by nonlinear growth paths on the  $D$ - $L$  diagram (i.e., 3-D PYFM conditions with constant fault height) [Schultz and Fossen, 2002; Polit *et al.*, 2005; Soliva *et al.*, 2005]. Cowie *et al.* [1994] describe fault populations at the East Pacific Rise (EPR) where brittle strain is distributed on nearly evenly spaced faults (Figure 2b), along which displacement profiles are flat topped [see Cowie *et al.*, 1994, Figure 8]. The fault system has been interpreted to indicate growth within (i.e., confined to) the oceanic brittle crust [Cowie, 1998; Bohnenstiehl and Kleinrock, 2000; Garel *et al.*, 2002]. These faults show nonlinear  $D_{\max}$ - $L$  scaling with a significant and progressive decrease in the  $D_{\max}/L$  ratio for the faults measured (Figure 2f) [Cowie *et al.*, 1994], suggesting that the brittle crust thickness controls the displacement maxima and displacement distributions on the faults. Figure 2f shows two 3-D scaling simulations produced using 3-D PYFM conditions for faults growing at constant height, consistent with a likely range of brittle crust thicknesses near the EPR [e.g., Bohnenstiehl and Carbotte, 2001]. The good correspondence between the 3-D scaling fits and the data (also observed at the Mid Atlantic Ridge for larger crust thickness, D. Bohnenstiehl (personal communication, 2007) suggests that the layer thickness is a major factor for the control of the fault system geometry [Cowie, 1998].

[15] It is also worth noting that intermediate cases, i.e., sublinear  $D_{\max}$ - $L$  scaling and nearly power law size distributions, were found in both crustal-scale continental and oceanic contexts, and therefore in rheologically inhomogeneous sequences [Marrett and Allmendinger, 1991; Scholz *et al.*, 1993; Scholz and Contreras, 1998; Bohnenstiehl and Kleinrock, 1999, 2000]. At smaller scale, a normal fault system at Canyonlands National Park (Utah, USA) exhibits average linear scaling although the strain is distributed along regularly spaced grabens [e.g., Trudgill and Cartwright, 1994]. In this case, ductile flow of evaporite-rich sediments beneath the faulted sedimentary sequence [Schultz-Ela and Walsh, 2002] may have promoted displacement accumulation nearly proportionally to fault length [Moore and Schultz, 1999]. It is thus possible that variations in viscosity (via strain rate or temperature profile changes) of a strongly inelastic lower unit underneath a faulted brittle layer may also affect fault displacement and strain localization [e.g., Bellahsen *et al.*, 2003], and can promote a variety of intermediate cases between the two end-members faulting regimes presented.

### 3. MER-Afar Transition Area

[16] In this section, we identify the two faulting regimes described above in different locations of the Main Ethiopian Rift (MER)-Afar area. We analyze fault spacing and linkage at relay ramps, as well as the fault size distribution, because as suggested in section 2, these attributes are the best indicators to reveal to which faulting regime a fault set belongs. Here we investigate currently active rift segments from the MER-Afar transition area, which is characterized

by exceptionally clear expression of normal fault traces over the whole topography of the region [Barberi *et al.*, 1975; Zanentini and Juste-Visentin, 1975; Gupta and Scholz, 2000a; Manighetti *et al.*, 2001]. Using the concepts presented in section 2, we analyze the surface traces of the normal fault scarps that were mapped using Landsat satellite images.

#### 3.1. Geological Setting

[17] The MER-Afar transition area forms the southern part of the triple junction between the Arabian, Nubian, and Somalian tectonic plates (Figure 3a). Plate motion has been partitioned between still active normal faulting in the East African rift (here the MER), the Gulf of Aden and Red Sea ridges, and by normal and recently sinistral faulting in the Afar depression [e.g., McKenzie *et al.*, 1970; Ayele, 1995; Hofstetter and Beyth, 2003]. Spreading has been interpreted to start  $\sim 10$  Ma or perhaps earlier in the Gulf of Aden [e.g., Cochran, 1981], and at 4–5 Ma in the Red Sea [e.g., Roeser, 1975], while the MER has remained continental since its initiation probably during the Oligocene [e.g., Pilger and Rösler, 1975; WoldeGabriel *et al.*, 1990; Ebinger *et al.*, 1993].

[18] The study area, exhibiting thousands of normal fault scarps [e.g., Gupta and Scholz, 2000a; Manighetti *et al.*, 2001], is located between latitudes  $9^{\circ}50'N$  and  $11^{\circ}50'N$ , which is the transition zone between the northern MER and the Goba'ad rift segments. The area is composed of (1) four distinct NNE striking rift segments (with individual topographic depressions due to faulting [Ebinger *et al.*, 1993]) of the north MER ( $S_{1-4}$  windows in Figures 3b and 3c), (2) a fault set of the Afar depression belonging to the NW striking Goba'ad rift segment (A), (3) a NNE Eastern MER border zone (B), and (4) a relatively elevated plateau area containing sub orthogonal fault sets and the WNW-ESE striking Goba'ad border zone (P-B). The studied faults are steeply dipping ( $\sim 70^{\circ}$ – $80^{\circ}$ ) and affect the subsurface Pliocene-Pleistocene stratoid basalts, cobble and tuff deposits, and Recent lacustrine-eolian sedimentary series [Taieb, 1975] (Figures 3c and 4 and also see Figures 5 and 6 for a more detailed view of the faults). The age of the faults observed at the surface is therefore  $<1.5$ – $1$  Ma. The faults also cut the Oligocene-Miocene trap series observed along the MER escarpments, and large rift segment border faults probably cut the entire brittle crust [Juch, 1975]. The mechanical stratification of the brittle crust is defined by 1- to 2-km-thick carapace of Ethiopian Traps, 700- to 800-m-thick Amba Aradam and Antalo-Gabreda Mesozoic marine series consisting mainly of limestones, sandstones and shales, and the Pan African basement below (Figure 4) [Juch, 1975; Pilger and Rösler, 1975].

[19] The onset of extension in the northern part of the MER has been recently dated to  $\sim 11$  Ma, i.e., more than 17 Ma after initial rifting in the southern Red Sea and Gulf of Aden [Wolfenden *et al.*, 2004]. The northwestern tip of the Gulf of Aden ridge (Asal and Goubet) and the southern lateral rift segments of the Red Sea ridge (Manda Hararo and Goba'ad segments) are interpreted to have propagated

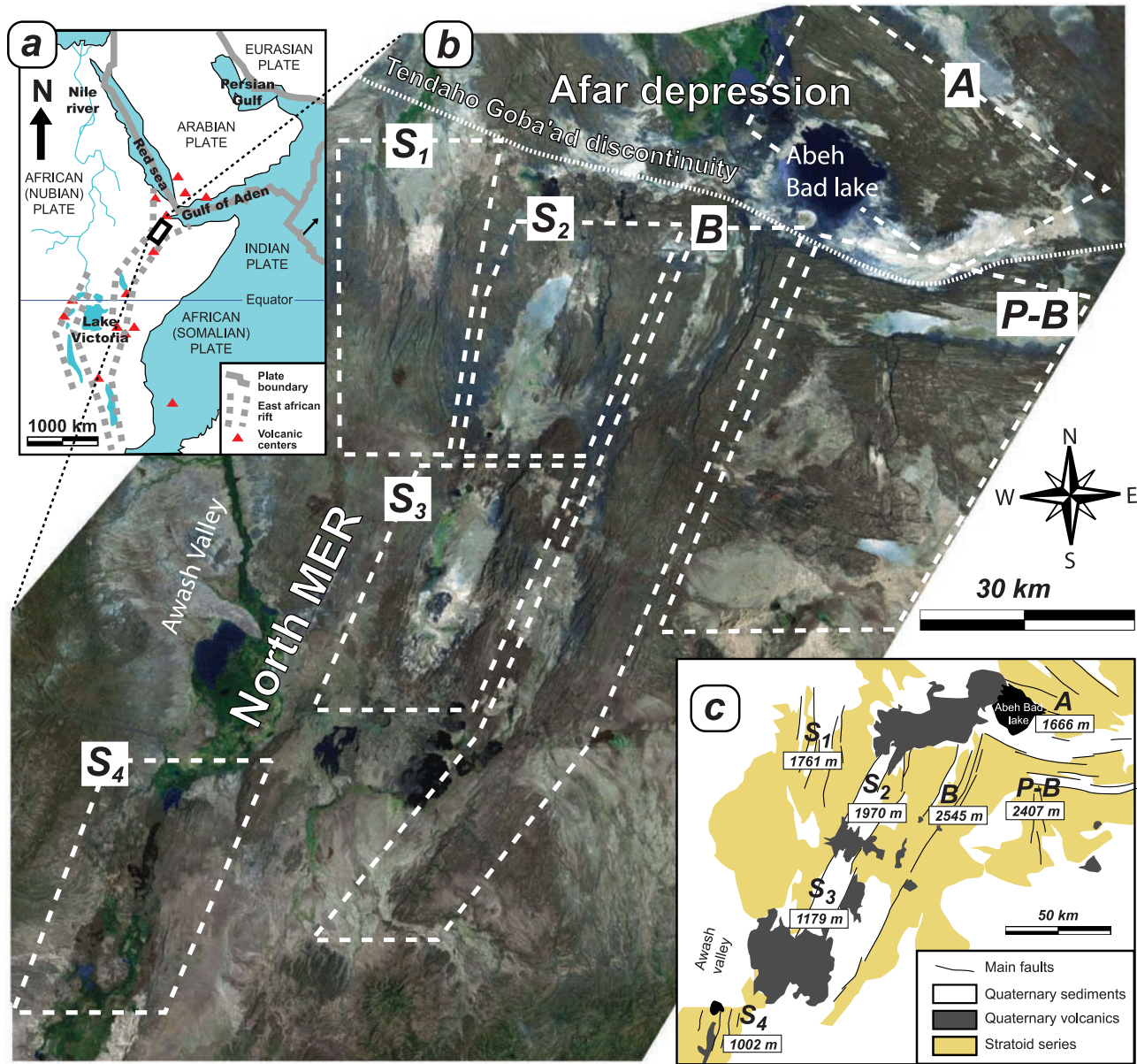


**Figure 3.** Overview of the Main Ethiopian Rift-Afar transition area. (a) General map of northeastern Africa. (b) Localization of the studied fault sets ( $S_1$ ,  $S_2$ ,  $S_3$ ,  $S_4$ , B, P-B, and A) in the studied region. (c) Simplified structural scheme of the studied area. Values are estimated basalt thicknesses from the fault geometrical attributes (see section 4.1 for explanations).

recently to the north of the MER and form the strict-sense Afar depression [Tapponier *et al.*, 1990; Sigmundsson, 1992; Lahitte *et al.*, 2003]. The Tendaho-Goba’ad discontinuity separates the northern MER with a NNE-SSW trend from the perpendicular Goba’ad rift segment with a WNW-ESE trend (Figure 3b).

[20] The actual seismicity in the still continental MER crust is consistent with NW-SE extension, with sparse earthquakes generally shallower than 10 km [Kebede and Kulhanek, 1991; Ayele *et al.*, 2004; Keir *et al.*, 2006]. In the

studied northern part of the MER, the seismicity is consistent with the main NNE-SSW extension driving the Tendaho-Goba’ad rift segment’s propagation [Ayele, 1995; Hofstetter and Beyth, 2003]. The eastern part of the Tendaho Goba’ad discontinuity (i.e., south of Abeh Bad lake) is highly seismically active as mainly normal-slip events accommodated along the WNW-ESE normal faults. The recent strike-slip motions registered along earlier normal fault scarps from the north of the Goba’ad region are interpreted as the result of large-scale horizontal block

Thicknesses	Age	Lithology	Comments
0 - 800 m and frequently absent	Actual - Holocene Pleistocene		Lacustrine, eolian sediments and volcanic rocks Salts, sands, sandstones, clays, basaltic and rhyolitic lava flows, pyroclastics Mainly observed faulted surface
Up to 1 km	Pleistocene - Pliocene		Acid Afar series Basalts, pyroclastics, ignimbrite, tuffs, silts, sandstones, conglomerates, limestones Stratoid series
1-2 km	Miocene and Oligocene floods		Upper Ethiopian traps Main silicic formation (Rhyolites and tuffs) Lower Ethiopian traps Massive volcanic rocks
	Possible Eocene floods		
~ 800 m	Cretaceous		Amba Aradam Sandstones Marls and Evaporites Sandstones Mainly Marine sedimentary rocks
	Jurassic		Gabreda Limestones Gabreda Marls
	Triassic		Gabreda - Antalo limestones Antalo shales Sandstones
?	Precambrian		Metamorphic basement

Figure 4. Synthesis of the stratigraphy in the MER-Afar transition area (see references in the text).

rotation between the recent Asal-Gouhbet and Tendaho-Goba’ad active rift propagators [Tapponier *et al.*, 1990; Sigmundsson, 1992; Manighetti *et al.*, 2001].

[21] In summary, the NNE-SSW normal faults from the north MER (in  $S_{1-4}$ , B and P windows, Figure 3b) result from WNW-ESE extension during the last 1.5 Ma, and were recently reactivated in strike-slip motion. By contrast, the recent WNW-ESE normal faults (in P-B and A windows) result from a Quaternary NNE-SSW extension associated to the Goba’ad rift segment propagation.

**3.2. Analysis and Data Acquisition**

[22] Our analysis permits the distinction of the different sets of faults described in section 3.1 (zones  $S_{1-4}$ , B, A and P-B, Figure 3b). We base our quantitative analysis of faults using map traces and measurements of fault spacing, overlap, and lengths on high-resolution satellite images.

The normal fault traces were mapped on ETM+ (Enhanced Thematic Mapper Plus) Landsat 7 images, which are 15-m-resolution panchromatic bands of the Earth’s surface (source for this data set is Global Land Cover Facility). This horizontal resolution corresponds to the minimum photographic bias for fault detection, defined as the truncation bias, which has been estimated up front and not interpreted from the fault statistics. A summary of the problem resulting from interpreted detection bias is given in Figure 7. A fault trace is identified on the satellite images by the change in fault pixel opacity and its specific rectilinear and segmented shape compared to the other geomorphologic elements. We assume that a pixel becomes opaque when two thirds of its surface are covered by a fault scarp trace (~10-m-thick horizontal trace). This assumption is particularly reliable for the identification of lineaments since they appear as aligned opaque pixels. Therefore a fault is estimated to be detected

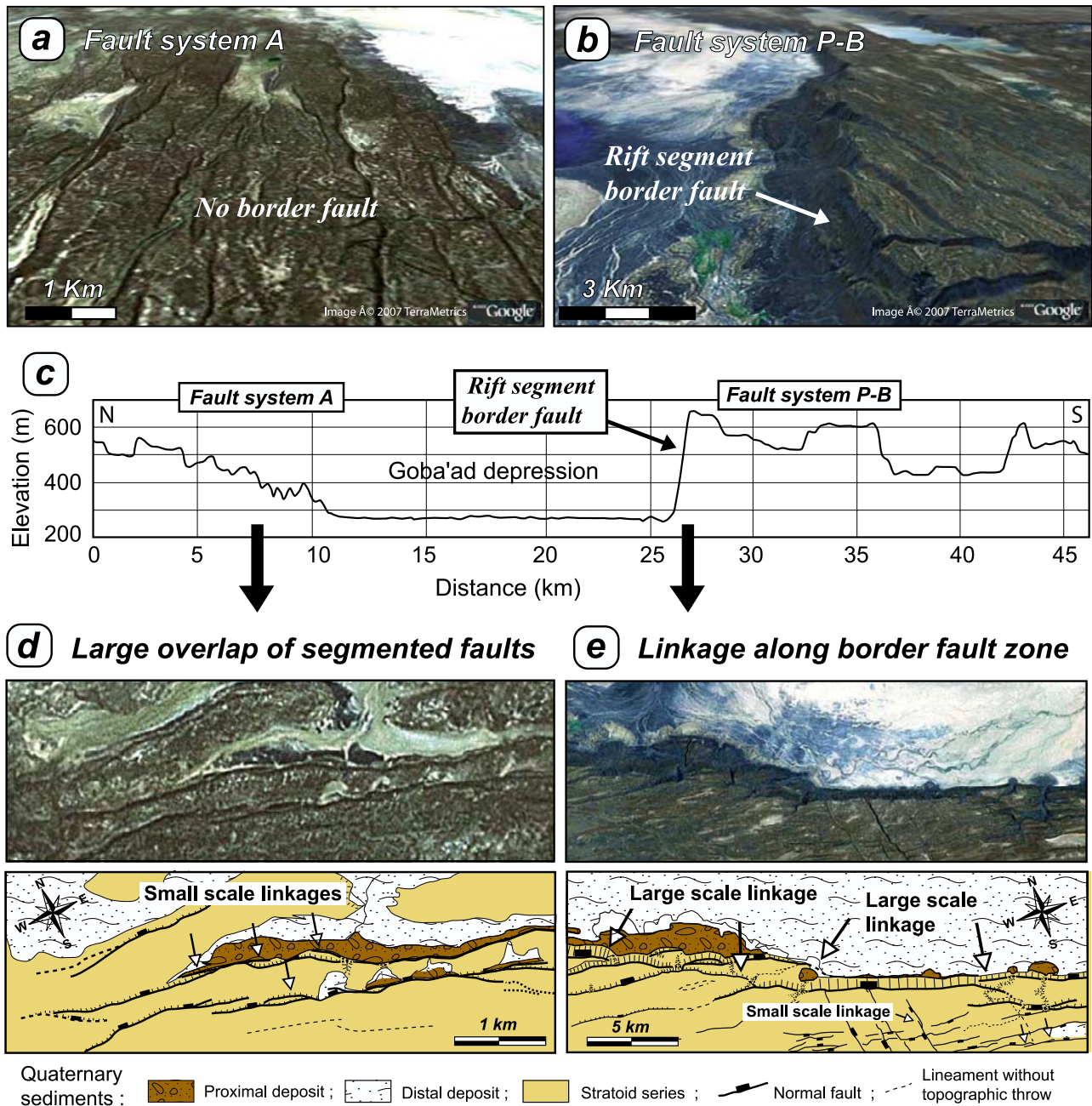


**Figure 5.** Satellite images and topography of areas showing distributed and localized faulting. Overview of (a) fault set A and (b) fault set P-B in 3-D perspective visualization. (c) NW-SE topographic cross section through the Goba’ad depression. Details of Landsat image and interpretation in (d) fault system A and (e) the Goba’ad border zone in map views. Note the difference in fault throw, distribution, and scale of fault linkage between the two fault sets.

since the fault throw is of equivalent dimension  $\sim 10$  m, assuming  $\sim 45^\circ$  degree talus composed of a scarp ( $70^\circ$ ) and stable deposits ( $30^\circ$ ). Using the average value of  $T_{max}/L$  ratio found by *Gupta and Scholz* [2000a] in the same area (0.015) and a fault throw of 10 m, we estimate that a reasonable truncation bias occurs for the length 600 m and then a resolution at fault end up to  $\sim 300$  m. In order to avoid any problem with truncation bias and to be unambig-

uously in the confidence interval of fault detection we increased this lower limit of fault detection to the round value of 1000 m (see Figure 7b). This can be done because of the sufficient number and large dimension of the faults in this region. Note that a combination of the images with shuttle radar topography mission (SRTM) digital elevation models (DEM, 10 m vertical resolution, then of equivalent truncation bias) was used to have overviews of the topog-

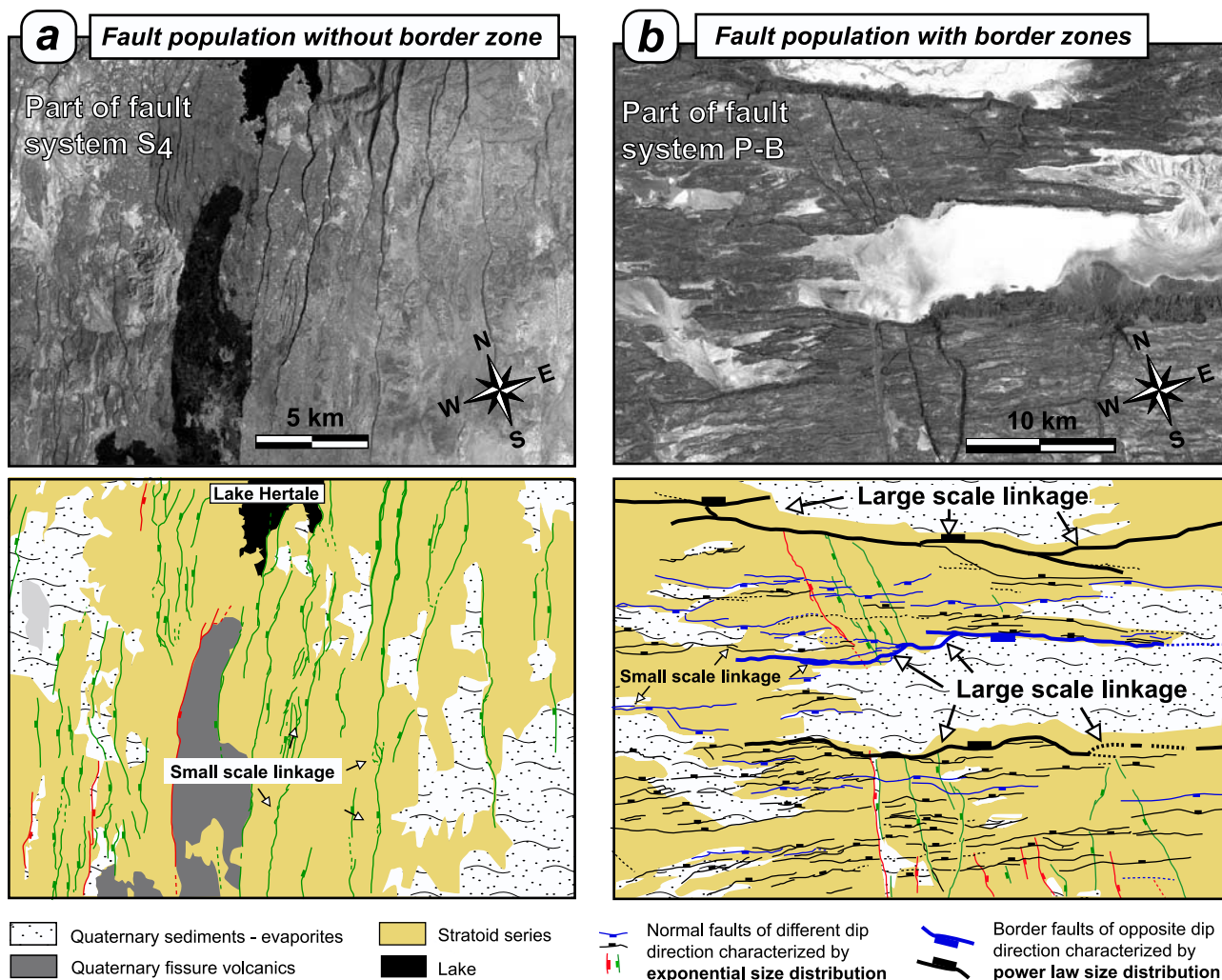


**Figure 6.** Landsat image and interpretations in map view of distributed and localized faulting in large windows of (a) fault system S<sub>4</sub> and (b) fault system P-B. Note the differences of fault lengths and the scale of fault linkage between the two fault sets.

raphy and determine the dip direction of the mapped faults. Lineaments larger than 600 m without topographic throw are assumed to be open fissures or drainage patterns.

[23] The problem of fault censoring (upper bias) is resolved by the very large size of the studied window (larger than the fault population for rift segments, Figure 3) and/or by explicitly referring which fault is censored by sediment infill or in rare cases by the end of the studied window on the size distribution graphs. All the faults have been checked and reported as an open symbol on graphs if censored. Figure 7 shows the advantage of this method, which permits a real evaluation of the scale range of confidence of fault sampling compared to commonly interpreted bias (Figures 2e and 7a) and therefore objectivity on the quality of the statistical fit function (Figure 7b).

[24] It is also important to note that we differentiate segmented (individual lengths) and linked array (total length) since we analyze the relationship between the scale

of fault linkage and size distributions. When fault segments are linked, we measure the entire (total) length of the fault segment array [e.g., Soliva and Benedicto, 2004; Soliva et al., 2006]. We do not consider the fault branches of the relay zones, which is (1) consistent with the process of fault branch abandon after segment linkage [e.g., Trudgill and Cartwright, 1994] and (2) because abandoned fault branches do not affect the behavior of the newly created fault.

### 3.3. Fault Population Analysis

[25] Overviews and satellite image analyses of the characteristic fault geometries observed in the studied area are presented in Figures 5 and 6. Some parts of rift segments exhibit distributed fault sets along multiple overlapping normal faults having little vertical throw (<200 m, e.g., fault set A in Figure 5 and fault set S<sub>4</sub> in Figure 6a). On the other hand, frequently closer to the rift segment center, large

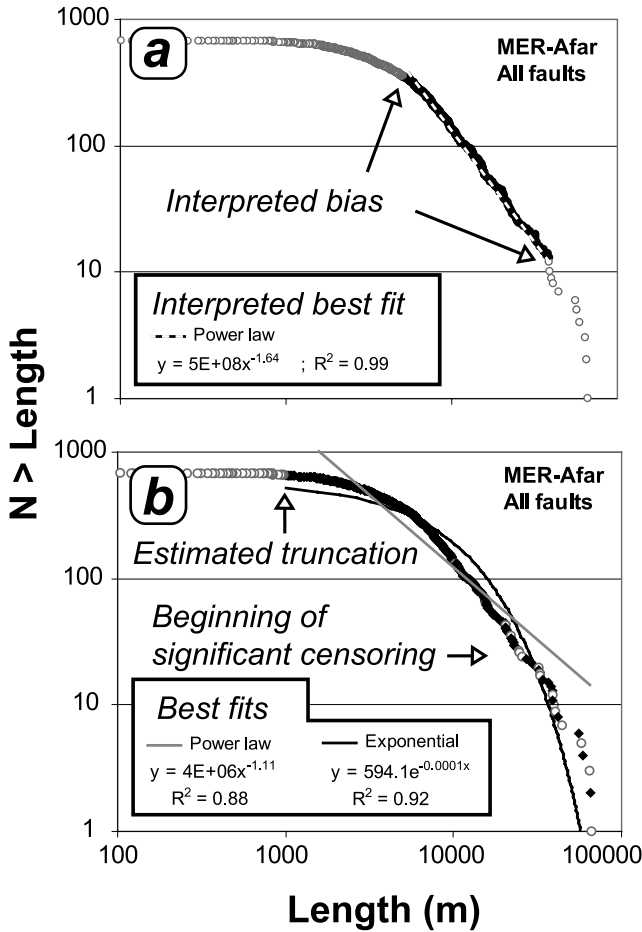


**Figure 7.** Cumulative size distribution of all the faults studied plotted together. (a) Best fit function along interpreted unbiased sample of the fault population is power law. (b) Power law and exponential fits along the real unbiased sample determined with satellite image analysis. Biased (white dots) and unbiased (black dots) data are distinguished. Fit functions are labeled on graphs. On such a diagram, including all the fault sets with determined bias, power law and exponential functions do not correctly fit the real unbiased sample.

inward facing faults (typically conjugate; see  $S_1$ ,  $S_2$  and  $S_3$  in Figure 3) form rift segment border faults implying strain localization with a maximum fault throw from 200 m and up to 600 m (e.g., fault set P-B in Figure 5), in which case the profile of topography is asymmetric (see the Goba’ad depression profile in Figure 5c). Some rare rift segments of smaller strain do not show these large border faults and are only composed of distributed strain along small throw faults (Figure 6a), as observed in parts of all other rift segments (e.g., Figures 5 and 6b). Most of the rift segments are primarily associated with distributed strain along little throw relatively short faults and localized strain along large faults (Figure 6b). This particular geometry of fault segmentation and size distribution is described quantitatively below.

[26] Figure 7 shows the cumulative size distribution frequency of all the faults studied. In Figure 7a we present the best fit (here a power law) of only the data belonging to a linear trend on log-log graph, whereas on Figure 7b, both exponential and power law best fits are presented for data contained between the estimated truncation and censoring bias. Figure 7 clearly shows that, depending on the sample used to fit a regression line, the power law can adequately explain the studied fault population. However, this data subset does not correspond to the full sample that can be taken with confidence, and therefore leads to an incorrect interpretation when using this apparent power law size distribution. The data sample that can be fit with confidence actually fails to reveal a good correlation with either power law or exponential relations.

[27] Relevant to the geometry of fault overlap and the spacing distance between which fault segments can link (see section 2), we consider that a fault can also bifurcate from a single plane into two branches, leading to an apparent linked relay. To avoid such a misinterpretation, for the linked segments on our overlap-separation graphs we only consider linked relays having (1) “hook” shape and not “Y” shape on map view, (2) subparallel faults linked by an oblique or perpendicular throughgoing fault, and (3) on the DEM, having a high topographic throw gradient along fault ends at the overlap zone. We also consider that the geometry of the linked relay zones could have been formed during late fault reactivation with a strike component of slip (see section 3.2). Calculations suggest that linkage is possible for a slightly larger scale for strike-slip fault tips than between normal fault tips [Crider and Pollard, 1998]. In this case, the spacing of the linked faults reported on graphs must be interpreted as the maximum possible spacing of linkage due to the normal fault development, i.e., the maximum spacing for the normal faults’ ability to link.

[28] Figure 8 shows the overlap separation data statistics of all the linked and unlinked overlapping faults in the studied area. This diagram shows that, although the unlinked overlapping faults show generally larger values of spacing and overlap than do linked faults, there is no clear sorting between these two sets. Using such a graphic without distinction between the different fault rift segments and fault systems suggests that the entire fault population is in appearance statistically close to a localized faulting regime (i.e., having unreal scale-invariant size distribution and segmentation, see Figures 7a and 2c for comparison), whereas faulting is widely distributed in the studied area (Figure 3). The brittle strain observed is distributed along different fault systems within a broad region of  $\sim 1000 \text{ km}^2$ , which questions the relevance of such global analyses of all faults in same graphs without distinctions. Below we demonstrate that the absence of clear sorting between linked and unlinked faults (Figure 8) and the apparent power law size distribution (Figure 7a) are due to the analysis of data combined from different areas and rift segments that actually require separate analyses.

[29] To investigate this issue, we present the data of overlap-separation and cumulative length frequency diagrams in Figures 9 and 10 for each mapping window shown

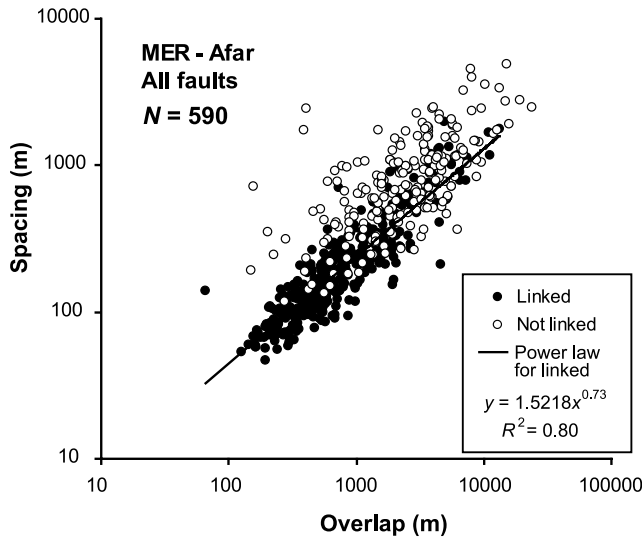


**Figure 8.** Spacing versus overlap data of all the faults studied plotted together. On such a diagram including all the fault sets, no limit of spacing for fault segment linkage is observed.

in Figure 3 (see section 3.2). Figure 9 shows that, in general, there is a sorting between the linked and unlinked overlapping faults. We statistically determine a critical value of spacing ( $S^*$ ) as the value of spacing having the same deviation factor ( $x$  labeled on the graphs) between each average spacing of linked and unlinked sets (see Appendix A for calculation). For example: for  $x = 1$  (i.e., the standard deviation  $1\sigma$ ),  $\sim 84\%$  of the white and black dots are respectively less and over  $S^*$ . For  $x = 2$ ,  $\sim 97.5\%$  of the white and black dots are respectively less and over  $S^*$ . It appears that this value can be quite different in each fault set and can vary as much as a factor of  $\sim 2.6$ .

[30] The quality and significance of the sorting between the linked and unlinked faults can be evaluated by the relative values of  $x$  (high  $x$  means a good sorting) and the “jump in the scale of linkage” ( $\delta$ , explicitly defined by the equation in Figure 9h). This jump  $\delta$  corresponds to the normalized difference between maximum spacing of linked faults and  $S^*$  (i.e., low  $\delta$  means no large-scale linkage). It is interesting that when a good sorting is observed between linked and unlinked faults (see especially Figure 9g, having very high  $x$  and relatively low  $\delta$ , and also Figures 9d with relatively high  $x$  and very low  $\delta$ ), the size distribution of the fault set is best fit by a negative exponential relation (Figures 10g and 10d). This shows quantitatively how fault linkage is restricted to a small spatial scale, which is marked by a different critical spacing in each case. In addition to these characteristics, the fault sets  $S_4$  and A show widely distributed strain along faults having small topographic throws; that is, there is no border fault localizing the brittle strain (Figures 5a, 5c, and 6a). Some examples of this small-scale fault linkage for the fault set A are presented in Figure 5d, in

which we recognize a very large overlap between unlinked faults (also see Figure 6a). These detailed fault system observations and scaling relations allow us to demonstrate the correlation between scale-dependent behavior and widely distributed strain summarized in section 2.

[31] On the other hand, other fault sets in the area show more ambiguous limits of linkage (see especially the fault set P-B, having very low  $\sigma$  and very high  $\delta$ , Figure 9f). These fault sets show size distributions that are much better explained by two best fits: An exponential distribution at small scale and a power law at large scale, rather than a single power or exponential fit (Figures 10a, 10b, 10c, 10e and 10f).

[32] The power law portion of the data is determined with the following condition: it must be a data sample fitting a power law with a least squares determination coefficient  $R^2 > 0.9$  within the (large) scale range containing all the border faults (noted by white arrows in Figures 9 and 10). Conversely, the exponential portion corresponds to the sample out of the power law portion, which is systematically best fit by a negative exponential function. Note that this fit always shows  $R^2 > 0.97$ . The power law size distribution can be either well developed (Figures 10e and 10f) or incipient (Figures 10b, 10c and caption text). Owing to the limited number of the faults used for the incipient power law fits in S2 and S3, the quantitative values in the equations and determination coefficients of these portions have no statistical strength, although the incipient linear trends (onset of power law) have obvious structural significance. There are actually few faults in these portions because they correspond to incipient border zones (not as well developed in S2 and S3 as in B, P-B or S1; see section 4.2 for the interpretation of the rift segments evolution). These samples, entirely composed of border faults, are linear and show clear steps from the exponential portions (also see section 4.2 for discussion on this step).

[33] It is important to note that all the power law portions contain a major proportion of large rift segment border faults (Figures 10a, 10b, 10c, 10e and 10f, and also see Figures 5b and 5c). These large faults contain the large-scale linked segments of Figures 9a, 9b, 9c, 9e and 9f (marked by an arrow). This jump in the scale of linkage and the scale-invariant behavior therefore both characterize the rift border zones (Figures 5b, 5c, 5e and 6b). An example of large-scale linkage along the Goba’ad border fault is shown in Figure 5e, along which coalescence occurs for spacing up to  $\sim 2$  km. Along these fault sets ( $S_1$ ,  $S_2$ ,  $S_3$ , B and P-B) we can thus identify the coexistence of distributed and localized faulting regimes. Figure 6b shows in map view the detailed pattern of a fault set that exhibits these two regimes. The border faults have large-scale linked segments that promote topographic throw localization along them. On the other hand, wide zones of distributed faulting around border faults are characterized by faults having small-scale linkage and large overlaps comparable (qualitatively and quantitatively) to the fault sets A and  $S_4$  (see Figures 5a, 5d and 6a).

[34] The results demonstrate that the statistics from the whole study area (Figures 7 and 10) combine different superposed trends (Figures 9 and 10). All faults on the

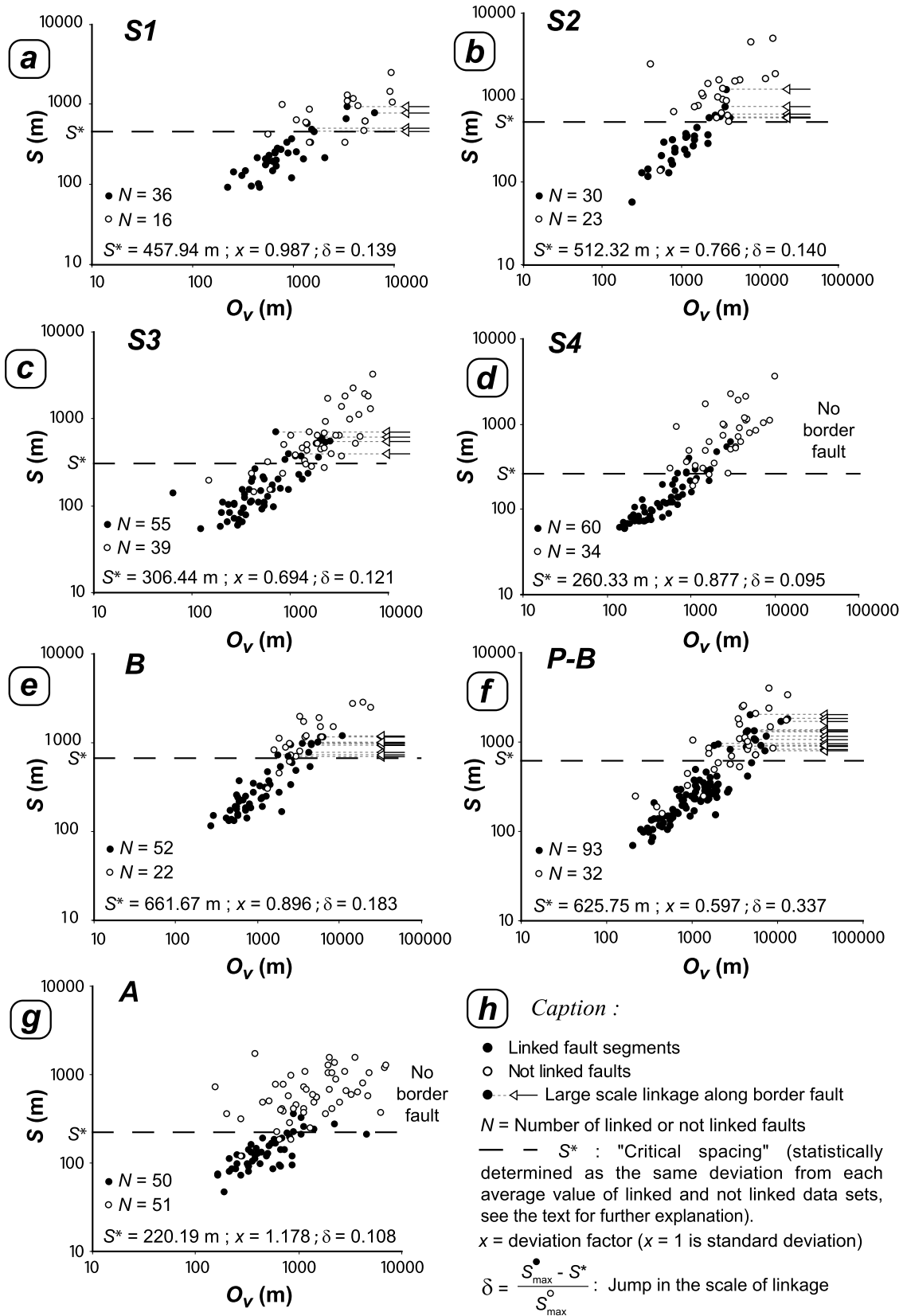


**Figure 9.** Spacing versus overlap graphs for the studied fault populations shown in Figure 3. Large-scale border faults are indicated on graphs. See the text for further details. Note the presence of variably expressed limit of spacing for fault segment linkage.

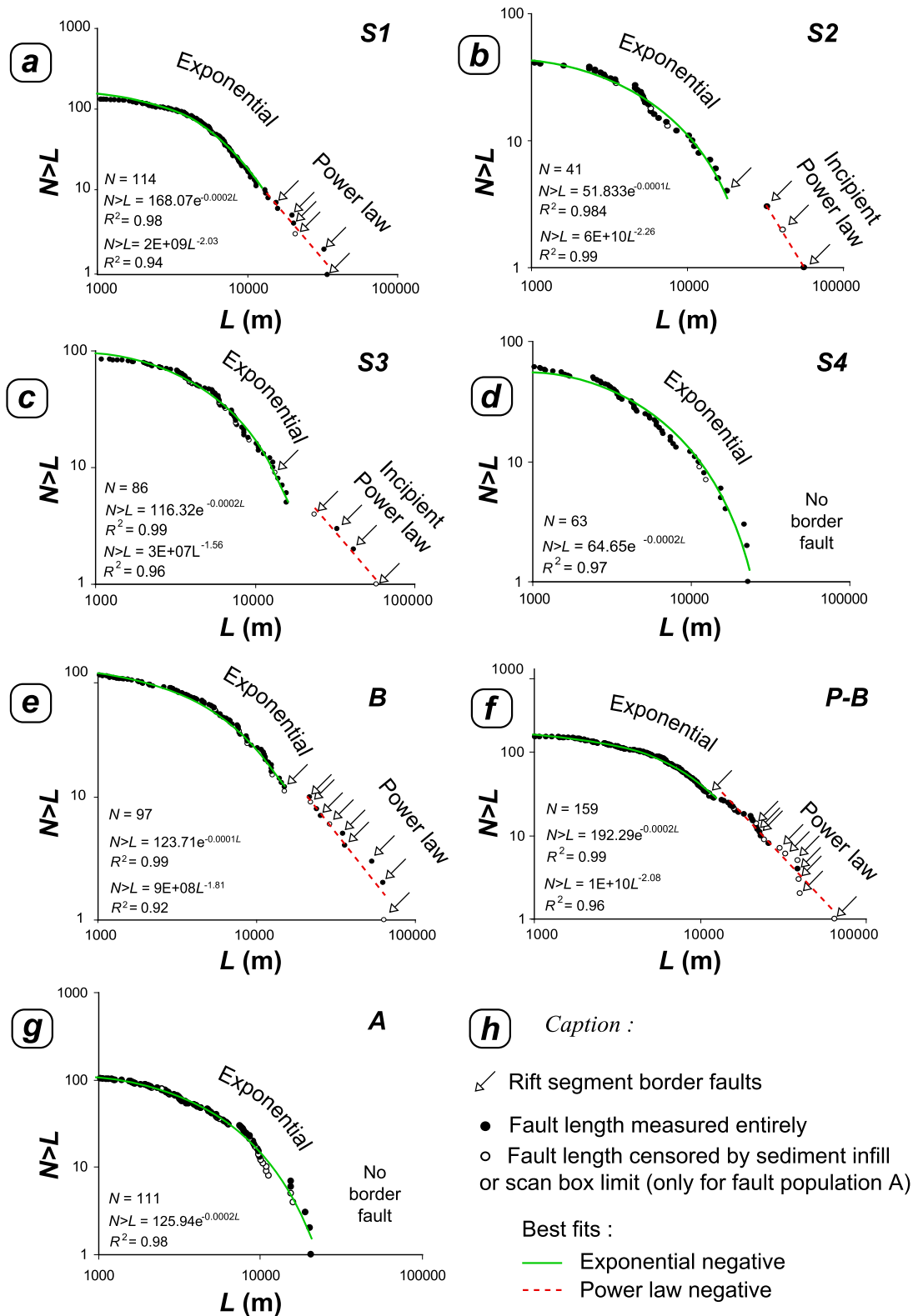


**Figure 10.** Cumulative size distribution graphs for the studied fault populations shown in Figure 3. Large-scale border faults are indicated on graphs. Truncated faults ( $L < 1000$  m) are not shown. Censored faults are indicated by white symbols. An “incipient” power law is defined when less than 10 faults are used for the fit; see the text for further details and the validity of the fits. Note the presence of real unbiased multi exponential and power law trends.

same graph of size distribution define a multi exponential size distribution (different scales of characteristic lengths) with a small component of the data better fitting power law trends which are inherent to each region. This results in an apparent power law with a smooth deflection for small faults that could, in the absence of detailed study of the individual fault geometries such as done in this paper, be misinterpreted as a truncation bias (Figure 7). This study area provides reliable examples of the coexistence of both distributed and localized faulting regimes in the Earth's crust [Gupta and Scholz, 2000a]. We have shown that the localized faulting regime corresponds to large-scale fault linkage and power law size distribution inherent to the rift segment border zones, whereas distributed faulting reflects widely overlapping smaller throw faults covering wide areas with exponential size distribution around the border faults. A given rift segment is therefore spatially characterized by a jump in the scale of fault linkage that contains information on its rheology, structure, and history.

## 4. Discussion

### 4.1. Depth of Faulting

[35] In section 2, we have shown that, in all the cases of distributed faulting regimes (i.e., fault populations characterized by a negative exponential size distribution and a critical spacing for fault linkage), the fault system is confined to a mechanical layer [e.g., Cowie *et al.*, 1994; Spyropoulos *et al.*, 1999; Ackermann *et al.*, 2001; Schultz and Fossen, 2002; Soliva *et al.*, 2006]. Although the scale of deformation, the structural context (rift system), and the lithology (basalts in the continental crust) are different than the examples presented in section 2.2, the MER-Afar transition area exhibits a large part of the brittle strain in a similar scale-dependent manner. We therefore infer that a significant proportion of the faults observed at the MER-Afar transition are confined to brittle mechanical layers. Since the degree of heterogeneity between layers has no significant effect on the variability of the values of  $S^*$  compared to the thickness of the mechanical layer [Bai and Pollard, 2000; Soliva *et al.*, 2006], we suggest that such a mechanical layer should be of different thickness in each studied fault set. Soliva *et al.* [2006], from a numerical approach, proposed a theoretical relation between the critical spacing and the thickness of the mechanical layer confining the faults, consistent with an empirical relation based on different fault systems on a broad range of scales. Using this relation (the mechanical layer thickness  $T = S^*/(0.26 \pm 0.016)$ ), we have estimated the values of mechanical thickness in each studied fault set (Figure 3c). We find a depth of faulting progressively increasing from  $\sim 1.76$  km ( $S_1$ ) in the west to  $\sim 2.54$  km (P-B) and 2.40 km (P) in the east. Using the maximum thickness expected in this eastern area, the fault depth decreases toward the north to  $\sim 1.66$  km in the Abeh Bad region (A) with a more gradual decrease toward the southwest along the MER axis to  $\sim 1$  km ( $S_4$ ).

[36] All the depths estimated from the distributed faulting regime unambiguously indicate intra brittle crust mechanical units. In the stratigraphy of the MER-Afar transition area

(Figure 4), the volcanic series appears as the unique potential candidate to behave as a mechanical unit of this kilometric (1–2.5 km) scale of thickness. The Trap series is mainly a series of massive flood basalts that erupted in two main pulses (Eocene-Oligocene and Miocene [Courtilot *et al.*, 1999; Baker *et al.*, 1996]). It is documented as originally covering an area in excess of 500,000 km<sup>2</sup> [Mohr and Zanettin, 1988] and formed a 1- to 2-km-thick carapace of flood basalts over the MER-Afar depression [e.g., Baker *et al.*, 1996; Hofmann *et al.*, 1997].

[37] As mentioned in section 3.3, 200 m is the maximum value of surface throw for the “nonborder zone” faults, i.e., the faults interpreted as cutting the traps and not the entire brittle crust. Using a fault downdip height  $H = 2000$  m, calculated for a minimum basalt thickness of 1.7 km (500 m stratoid + a minimum of 1200 m traps) and a fault dip of  $60^\circ$ , the maximum downward displacement gradient found is  $D_{\max}/H = 200/2000 = 0.1$ . Because the faults cut the Earth's surface, this value can be considered as the displacement gradient of a half fault. The common (statistical) values of different types and systems of faults have been documented in the literature to be approximately  $D_{\max}/L = 0.03$  [e.g., Schlische *et al.*, 1996; Schultz and Fossen, 2002]. To compare our vertical gradient (i.e., half fault) with the  $D_{\max}/L$  ratio of the literature we must consider the value  $D_{\max}/2H = 0.05$ . This value is consistent with typical fault gradients (i.e., a little higher than 0.03), first because we consider the maximum value observed on all the “nonborder zone” faults, but also because downdip gradients are commonly larger than typical along-strike gradients in horizontal series of layered rocks [Wilkins and Gross, 2002; Soliva and Benedicto, 2005; Soliva *et al.*, 2006].

[38] In addition to this estimate of the amount of displacement, field observations are consistent with strain decoupling at the base of the Traps. Juch [1975] documents the geometry of tilted blocks along the southeastern Ethiopian escarpment (major border fault zone), with many faults that do not cut entirely the Gabreda Antalo limestone series. It is therefore possible that in the MER-Afar transition area this unit has decoupled the brittle strain above by restricting downward propagating faults initiated in the overlying brittle Traps.

[39] On the other hand, the faults that are characterized by power law size distribution and large-scale linkage, which belong to border zones (large throw faults), should be of much larger depth and perhaps cut the entire brittle crust. This inference is supported by the spacing between conjugate border faults in rift segments (5–6 km spacing) that probably intersect close to the base of the brittle crust (probably 5–6 km depth). With respect to a half fault downward displacement of 0.1 (see above), we expect a fault depth to  $\sim 5.2$  km (i.e., a fault height of 6 km and  $60^\circ$  dip) using a value of fault displacement of 600 m. This maximum value of throw observed on border faults is potentially an underestimate of displacement due to erosion and sediment infill (see Figure 5e). At the MER-Afar transition area the lithosphere is only represented by a thin crust, which is probably of  $\sim 10$  km thickness and potentially even thinner at the incipiently spreading rift seg-

ments [Kebede and Kulhanek, 1991; Ebinger et al., 1993]. Large-scale linkage and power law size distribution (as observed in the localized regime) is in the MER-Afar transition area a large-scale phenomenon (faults segments having  $L > 10$  km, Figure 10) and therefore quantitatively describes the process of continental rifting. The fact that large-scale linkage is favored along border faults of large topographic throw (e.g., Figures 5b and 9) is particularly well expressed along the border fault (in a strict sense) between the Asella-Sire and Arboye large fault segments of the southeastern MER escarpment. Keranen et al. [2004] show tomographic crustal fault sections in this area through what can be interpreted as one of the largest linked normal fault relays ever identified. Here the faults probably affect the entire layered crust overlying a hot and viscous mantle, producing a hierarchy of scales of normal faulting in the northern MER.

[40] Bellahsen et al. [2003] have shown, with both analogue and numerical simulations of elastic-brittle plate extension over a viscous material, that strain localization is enhanced for slow extension rates. For the northern MER, geodetic data indicate that the ESE-WNW extensional strain velocity over the period 1972–1992 is less than 8 mm/a [Asfaw et al., 1992], and in the Afar depression in the strict sense the NE-SW extension velocity (i.e., corresponding to the Arabia and Somalia plate separation) is less than 20 mm/a. In the study area, extensional strain velocities are relatively slow and are associated at the large scale (i.e., the faults that can be influenced by the viscous behavior of the lower crust) with localized faulting (Figure 1a). This localized style of continental extension contrasts with the distributed faulting behavior observed at mid-ocean ridges such as the East Pacific Rise.

#### 4.2. Four-Dimensional Rift Segment Evolution

[41] We have described the coexistence of two brittle strain regimes, their spatial distribution, and their origin in terms of mechanisms of fault growth. However, it is also important to discuss the temporal sequence of the faulting regimes observed. Although the differences in exponential and power law size distributions between the fault sets are due to variations in brittle crust heterogeneity, they also evolve with the amount of fault system strain [e.g., Cowie et al., 1995; Ackermann et al., 2001]. We observe that, where border fault zones are well developed (fault sets B and P-B, length  $>50$  km and  $\sim 500$  m topographic throw on fault zones less than 5 km wide, Figure 5), the size distribution shows a predominantly power law trend and a large scale of segmentation (Figures 9e, 9f, 10e, and 10f). Conversely, where border zones are less developed (less than 50 km in length,  $S_1$ ,  $S_2$  and  $S_3$ ), the power law part of the size distribution is less well expressed. Where border zones are absent, no power law size distribution is observed and an exponential function fits correctly the data.

[42] The observation of small throw faults cut by the large border faults (see Figure 5b) shows that the border zones formed late in the process, leading to the localization of faulting along several preexisting faults by large-

scale linkage (Figure 11). This sequence of fault development contrasts with scale-invariant system development, where stress shadowing around the largest faults inhibits fault nucleation and lateral propagation, leading to zones with few faults around the master (or border) faults [e.g., Aydin and Schultz, 1990; Cowie et al., 1995; Ackermann and Schlische, 1997; Cowie and Shipton, 1998]. The temporal sequence shown in Figure 11 is therefore a reasonable explanation for why faults with small topographic throw are frequently observed in the close vicinity of the border zone and sometimes linked with them (see Figures 5b, 5e, and 6b). In addition, this sequence of deformation can explain the details of fault segmentation along the border fault zones. First, large scatter is observed in values of  $O_v$ - $S$  (especially large  $O_v/S$  ratios up to  $\sim 10$ ) on several faults linked with the border faults (Figures 5e and 6b) compared to the values commonly observed for linked faults [e.g., Aydin and Schultz, 1990; Soliva and Benedicto, 2004]. Second, the border faults are composed of linked fault segments whose lengths are consistent with the maximum length observed in the exponential part of the size distribution (see the linked fault segments along the border faults of Figure 6b). The border faults were apparently initiated as part of distributed faults (vertically restricted) of the mechanical unit (stages 1 and 2, Figures 11b and 11c) that then coalesced during a later stage, forming border faults proper and thereby allowing crustal-scale strain localization (stage 3) (Figure 11d). This localization sequence (border zone formation) is consistent with the increase of fault depth and promotes an increase in the scale of fault linkage [see Soliva et al., 2006]. The up scaling of fault linkage allows the birth of few very large faults and therefore of the power law size distribution at large scale (Figure 11a). This sequence is marked by a clear step between the exponential and the incipient power law size distributions observed in Figures 10b, 10c and 10d, and corresponds to new large faults created by large-scale linkage (Figure 11d). Development of fault localization leading to the formation and propagation of the rift border zone probably attenuates this step by promoting fault linkage on a wider scale range, as observed in areas B and P-B (Figures 9 and 10).

[43] Our results show that MER-Afar rift border faults are characterized by large-scale fault linkage (Figure 11d). We therefore identify a transition from an exponential relation (consistent with faults contained within the basalt traps' thickness) to a subsequent power law relation when the faults cut a larger section of the crust (Figure 11a). This suggests that at large scale, a transition from exponential to power law is possible, which differs to the more limited case for faults entirely confined into a single layer [Ackermann et al., 2001; Soliva and Benedicto, 2005].

## 5. Conclusions

[44] Fault systems in extensional settings are characterized by localized or distributed patterns. Distributed faulting is characterized by an exponential size distribution and a critical maximum spacing for which fault

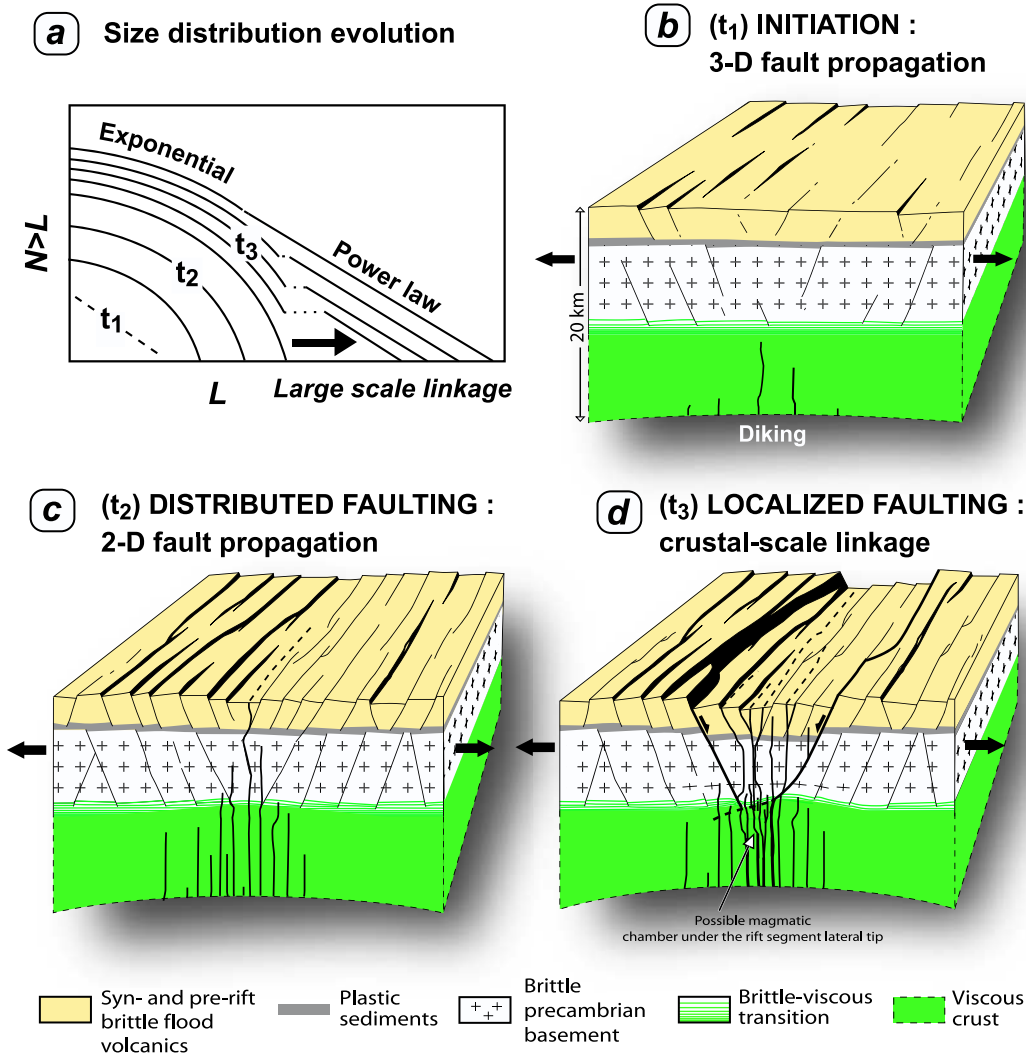


**Figure 11.** Interpretation of the evolution of a fault system at a rift segment. (a) Temporal sequence of the size distribution. (b) First stage ( $t_1$ ) of fault system formation. (d) Strain distribution ( $t_2$ ) in the mechanical units. Note that syntectonic sediments and surface basalt floods flowing from dikes (black vertical lines and dashed lines at the surface) are not shown for figure legibility. (d) Strain localization ( $t_3$ ) forming rift segment border zones by large-scale coalescence of pre-existing (formerly distributed) fault segments.

segments can link, whereas localized faulting is characterized by a power law size distribution and fault segments able to link at a larger range of scale. Their occurrence is dependent on the mechanical stratification of the deforming rock mass, and hence the minimum fault dimension, and these processes are observed in different structural settings as well in the sedimentary cover as at the crustal scale.

[45] The MER-Afar transition area reveals that both localized and distributed faulting can coexist in the same fault system, and that each one corresponds to a specific structure of the rift. Distributed faulting is observed in wide areas around rift segment border faults and is probably governed by the thickness of the brittle volcanic series (mainly Ethiopian traps and stratoid series). Local-

ized faulting associated with the rift segment border zones show fault segments able to link up at fault spacings up to a kilometeric scale. The formation of rift segment border zones is therefore characterized by a jump in the scale of segmentation and coalescence. The MER-Afar transition area exhibits strain localization along rift segment border faults in a context of relatively slow strain rates. This continental environment contrasts with the scale-dependent distributed strain behavior observed at mid oceanic ridges.

[46] These results are important for fault growth models and fault system geometry prediction, for which a scale-invariant regime has been assumed since the past decade. For example, it is obvious that in each faulting regime evaluated in this paper, the localization of the

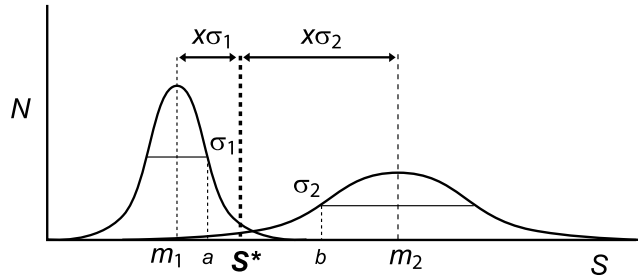


**Figure A1.** Schematic graph of  $N$  (number of faults) versus  $S$  (spacing) showing the graphical significance of all the parameters used in equations.

seismicity along isolated faults, between overstepping faults or in a longer term, along the entire fault system will be different since stress interactions and linkages are not necessarily self-similar.

[47] We have also shown that what appear to be censoring and truncation biases can actually be real scaling properties of the fault system. We propose that the confidence on the data sample used can be constrained by estimating the upper scale of truncation bias and indicating which fault is censored on the graphs. Multi-scale-dependent regimes can appear as a scale-invariant behavior on cumulative size distribution and  $D_{\max}$ - $L$  graphs if different fault system geometries are plotted together. Our work suggests that this problem can occur if the size of the study window is much larger than that of lateral variations of the rock rheology and fault system geometry. This is particularly important for any work attempting to discuss fault growth models, calculate brittle strain, or predict fault lengths on the basis of empirical scaling relations.

## Appendix A: Calculating $S^*$

[48] Here we show how the value of critical spacing ( $S^*$ ) is determined statistically between two populations of spacing data. Figure A1 shows a graph of  $N$  (number of data) versus  $S$  (spacing) with all the parameters needed for calculation.

## References

- Ackermann, R. V., and R. W. Schlische (1997), Anticlustering of small normal faults around larger faults, *Geology*, 25, 1127–1130.
- Ackermann, R. V., R. W. Schlische, and M. O. Withjack (2001), The geometric and statistical evolution of normal fault systems: An experimental study of the effects of mechanical layer thickness on scaling laws, *J. Struct. Geol.*, 23, 1803–1819.
- Asfaw, L., R. Bilham, M. Jackson, and P. Mohr (1992), Recent inactivity across the African Rift, *Nature*, 357, 447.
- Audin, L., P. Tapponnier, I. Manighetti, F. Métivier, and P. Huchon (2001), Fault propagation and climatic control of sedimentation on the Ghoubbet Rift floor: Insights from the Tadjouraden cruise in the western gulf of Aden, *Geophys. J. Int.*, 144, 391–413.
- Aydin, A., and R. A. Schultz (1990), Effect of mechanical interaction on the development of strike-slip fault with an echelon patterns, *J. Struct. Geol.*, 12, 123–129.
- Ayele, A. (1995), Earthquake catalogue of the Horn of Africa for the period 1960–93, *Rep.* 3-95, 32 pp., Seismol. Dep., Uppsala Univ., Uppsala, Sweden.
- Ayele, A., A. A. Nyblade, C. A. Langston, M. Cara, and J.-J. Leveque (2004), The May 2000 earthquake swarm near Gewane in south Afar, in *Proceedings of International Conference on the East African Rift System*, edited by G. Yirgu et al., pp. 23–25, Ethiopian Geosci. and Miner. Eng., Addis Ababa, Ethiopia.
- Bai, T., and D. D. Pollard (2000), Fracture spacing in layered rocks: A new explanation based on the stress transition, *J. Struct. Geol.*, 22, 43–57.
- Baker, J., L. Snee, and M. Menzies (1996), A brief Oligocene period of flood volcanism in Yemen: Implications for the duration and rate of continental flood volcanism at the Afro-Arabian triple junction, *Earth Planet. Sci. Lett.*, 138, 39–55.
- Barberi, F., G. Ferrara, R. Santacroce, and J. Varet (1975), Structural evolution of the Afar triple Junction, in *Afar Depression of Ethiopia*, edited by A. Pigler and A. Rosler, pp. 38–54, E. Schweizerbart'sche, Stuttgart, Germany.
- Bellahsen, N., J.-M. Daniel, L. Bollinger, and E. Burov (2003), Influence of viscous layers on growth of normal faults: Insights from experimental and numerical models, *J. Struct. Geol.*, 25, 1471–1485.
- Bohnenstiehl, D. R., and S. M. Carbotte (2001), Faulting patterns near 19°30'S on the East Pacific Rise: Fault formation and growth at a superfast spreading

[49]  $S^*$  is calculated from means ( $m_1$ ,  $m_2$ ) and standard deviations ( $\sigma_1$ ,  $\sigma_2$ ) values from both populations of spacing values. From Figure A1,  $S^*$  can be explicitly written as

$$S^* = \left[ \frac{\sigma_1}{\sigma_1 + \sigma_2} \cdot (b - a) \right] + a. \quad (A1)$$

The positions on abscissa of the values  $a$  and  $b$  are explicited by

$$a = m_1 + \sigma_1 \quad (A2)$$

$$b = m_2 - \sigma_2. \quad (A3)$$

Substituting equations (A2) and (A3) into (A1) gives

$$S^* = \left[ \frac{\sigma_1 m_2 - \sigma_1 \sigma_2 - \sigma_1 m_1 - \sigma_2^2}{\sigma_1 + \sigma_2} \right] + m_1 + \sigma_1. \quad (A4)$$

This equation was used to calculate  $S^*$  in Figure 9.

[50]  $S^*$  can also be written as a function of  $x\sigma_1$  and  $x\sigma_2$  such as

$$S^* = m_1 + x\sigma_1 \quad (A5)$$

$$S^* = m_2 - x\sigma_2. \quad (A6)$$

These equations were used to calculate  $x$  in Figure 9. Here  $x = 1$  means  $S^*$  is determined at the standard deviations  $\sigma_1$  and  $\sigma_2$  from  $m_1$  and  $m_2$ , respectively. Since the standard deviation explains  $\sim 68\%$  of the data,  $\sim 84\%$  ( $68 + 32/2$ ) of the white and black dots are respectively less and over  $S^*$ ;  $x$  is therefore an indicator of the quality of data sorting between the two spacing populations.

[51] **Acknowledgments.** The main part of this work was done during a postdoctoral stay with the Geomechanics Rock Fracture Group (exchange research program P-1-03572) at the University of Nevada, Reno (USA). The work was supported by NASA grants to Richard Schultz. Discussions with Hermann Zeyen, Yves Lagabriele, and Maurice Mattauer were fruitful. We thank Del Wayne Bohnenstiehl and Patience Cowie for providing data from the East Pacific Rise, and Tatiana Tentler, Del Wayne Bohnenstiehl, and Robert Holdsworth for their constructive comments on the manuscript.

- center, *Geochem. Geophys. Geosyst.*, 2(9), doi:10.1029/2001GC000156.
- Bohnenstiehl, D. R., and M. C. Kleinrock (1999), Faulting and fault scaling on the median valley floor of the Trans-Atlantic Geotraverse (TAG) segment, 26°N on the Mid-Atlantic Ridge, *J. Geophys. Res.*, 104, 29,351–29,364.
- Bohnenstiehl, D. R., and M. C. Kleinrock (2000), Evidence of spreading-rate dependence in the displacement-length ratios of abyssal hill faults at mid-ocean ridges, *Geology*, 28, 395–398.
- Brun, J.-P. (1999), Narrow rifts versus wide rifts: Inferences for the mechanics of rifting from laboratory experiments, *Philos. Trans. Roy. Soc., Ser. A*, 357, 695–712.
- Buck, W. R. (1991), Modes of continental lithospheric extension, *J. Geophys. Res.*, 96, 20,161–20,178.
- Carbotte, S. M., and K. C. Macdonald (1994), Comparison of seafloor tectonic fabric at intermediate, fast, and super fast spreading ridges: Influence of spreading rate, plate motions, and ridge segmentation on fault patterns, *J. Geophys. Res.*, 99, 13,609–13,631.
- Cladouhos, T. T., and R. Marrett (1996), Are fault growth and linkage models consistent with power-law distributions of fault lengths?, *J. Struct. Geol.*, 18, 281–293.
- Clark, R. M., and S. J. D. Cox (1996), A modern regression approach to determining fault displacement-length relationships, *J. Struct. Geol.*, 18, 147–152.
- Cochran, J. R. (1981), The Gulf of Aden: Structure and evolution of a young ocean basin and continental margin, *J. Geophys. Res.*, 86, 263–287.
- Corti, G., M. Bonini, S. Conticelli, F. Innocenti, P. Manetti, and D. Sokoutis (2003), Analogue modelling of continental extension: A review focused on the relations between the patterns of deformation and the presence of magma, *Earth Sci. Rev.*, 63, 169–247.
- Courtilot, V., C. Jaupart, I. Manighetti, P. Tapponnier, and J. Besse (1999), On causal links between flood basalts and continental breakup, *Earth Planet. Sci. Lett.*, 166, 177–195.
- Cowie, P. A. (1998), Normal fault growth in three dimensions in continental and oceanic crust, in *Faulting and Magmatism at Mid-Ocean Ridges*, *Geophys. Monogr. Ser.*, vol. 106, edited by R. Buck et al., pp. 325–348, AGU, Washington, D. C.
- Cowie, P. A., and C. H. Scholz (1992), Physical explanation for the displacement-length relationship of fault using a post-yield fracture mechanics model, *J. Struct. Geol.*, 14, 1133–1148.
- Cowie, P. A., and Z. K. Shipton (1998), Fault tip displacement gradients and process zone dimensions, *J. Struct. Geol.*, 20, 983–997.
- Cowie, P. A., A. Malinverno, W. B. F. Ryan, and M. H. Edwards (1994), Quantitative fault studies on the East Pacific Rise: A comparison of sonar imaging techniques, *J. Geophys. Res.*, 99, 15,205–15,218.
- Cowie, P. A., D. Sornette, and C. Vanneste (1995), Multifractal scaling properties of a growing fault population, *Geophys. J. Int.*, 122, 457–469.
- Crider, J. G., and D. D. Pollard (1998), Fault linkage: Three-dimensional mechanical interaction between echelon normal fault, *J. Geophys. Res.*, 103, 24,373–24,391.
- Dawers, N. H., M. H. Anders, and C. H. Scholz (1993), Growth of normal faults: Displacement-length scaling, *J. Struct. Geol.*, 21, 1107–1110.
- dePolo, C. M. (1998), A reconnaissance technique for estimating the slip rates of normal-slip faults in the Great Basin, and application to faults in Nevada, USA, Ph.D. thesis, 223 pp., Univ. of Nev., Reno.
- Ebinger, C. J., T. Yemane, G. Woldegabriel, J. L. Aronson, and R. C. Walter (1993), Late Eocene–Recent volcanism and faulting in the southern main Ethiopian rift, *J. Geol. Soc.*, 150, 99–108.
- England, P. C. (1983), Constraints on extension of continental lithosphere, *J. Geophys. Res.*, 88, 1145–1152.
- Fletcher, R. C., and B. Hallet (1983), Unstable extension of the lithosphere: A mechanical model for Basin-and-Range structure, *J. Geophys. Res.*, 88, 7457–7466.
- Garel, E., O. Dautiel, and Y. Lagabrielle (2002), Deformation processes at fast to ultra-fast oceanic spreading axes: Mechanical approach, *Tectonophysics*, 346, 223–246.
- Gross, M. R., G. Gutiérrez-Alonso, T. Bai, M. A. Wacker, K. B. Collinsworth, and R. J. Behl (1997), Influence of mechanical stratigraphy and kinematics on fault scaling relations, *J. Struct. Geol.*, 19, 171–183.
- Gupta, A., and C. H. Scholz (2000a), Brittle strain regime transition in the Afar depression: Implication for fault growth and seafloor spreading, *Geology*, 28, 1087–1090.
- Gupta, A., and C. H. Scholz (2000b), A model of normal fault interaction based on observation and theory, *J. Struct. Geol.*, 22, 865–879.
- Handy, M. R. (1989), Deformation regimes and the rheological evolution of fault zones in the lithosphere: The effects of pressure, temperature, grain size, and time, *Tectonophysics*, 163, 119–152.
- Hofmann, C., G. Courtillot, P. Féraud, G. Rochette, E. Yirgou, Ketefo, and R. P. (1997), Timing of the Ethiopian flood basalt event and implications for plume birth and global change, *Nature*, 389, 838–841.
- Hofstetter, R., and M. Beyth (2003), The Afar depression: Interpretation of the 1860–2000 earthquakes, *Geophys. J. Int.*, 155, 715–732.
- Hopper, J. R., and W. R. Buck (1996), The effect of lower crustal flow on continental extension and passive margin formation, *J. Geophys. Res.*, 101, 20,175–20,194.
- Hu, M. S., and A. G. Evans (1989), The cracking and decohesion of thin films on ductile substrate, *Acta Mater.*, 37, 917–925.
- Juch, D. (1975), Geology of the southeastern escarpment of Ethiopia between 39 and 42 longitude east, in *Afar Depression of Ethiopia*, *Sci. Rep.*, vol. 4, edited by A. Pilger and A. Rosler, pp. 310–316, Schweizerbart, Stuttgart, Germany.
- Kakimi, T. (1980), Magnitude-frequency relation for displacement of minor faults and its significance in crustal deformation, *Bull. Geol. Surv. Jpn.*, 31, 467–487.
- Kebede, F., and O. Kulhanek (1991), Recent seismicity of the East African rift system and its implication, *Phys. Earth Planet. Inter.*, 68, 259–273.
- Keranen, K., S. L. Klempner, and R. Gloaguen (2004), Imaging a proto-ridge axis in the Main Ethiopian Rift, *Geology*, 32, 949–952.
- Keir, D., C. Ebinger, G. Stuart, E. Daly, and A. Ayele (2006), Strain accommodation by magmatism and faulting as rifting proceeds to breakup: Seismicity of the northern Ethiopian rift, *J. Geophys. Res.*, 111, B05314, doi:10.1029/2005JB003748.
- Kim, Y. S., and D. J. Sanderson (2005), The relationship between displacement and length of faults: A review, *Earth Sci. Rev.*, 68, 317–334.
- Knott, S. D., A. Beach, P. J. Brockbank, J. L. Brown, J. E. McCallum, and A. I. Welbon (1996), Spatial and mechanical controls on normal fault populations, *J. Struct. Geol.*, 18, 359–372.
- Kohlstedt, D. L., B. Evans, and S. J. Mackwell (1995), Strength of the lithosphere: Constraints imposed by laboratory experiments, *J. Geophys. Res.*, 100, 17,587–17,602.
- Koledoye, A. B., A. Aydin, and E. May (2000), Three dimensional visualization of normal fault segmentation and its implication for fault growth, *Leading Edge*, 19, 691–701.
- Lahitte, P., P.-Y. Gillot, and V. Courtillot (2003), Silicic central volcanoes as precursors to rift propagation: The Afar case, *Earth Planet. Sci. Lett.*, 207, 103–116.
- Lin, J., and E. M. Parmentier (1988), Quasistatic propagation of a normal fault: A fracture mechanics model, *J. Struct. Geol.*, 10, 249–262.
- Maerten, L., P. Gillespie, and D. D. Pollard (2002), Effect of local stress perturbation on secondary fault development, *J. Struct. Geol.*, 24, 145–153.
- Main, I. G., P. G. Meredith, P. R. Sammonds, and C. Jones (1990), Influence of fractal flaw distributions on rock deformation in the brittle field, in *Deformation Mechanisms, Rheology and Tectonics*, edited by R. J. Knipe and E. H. Rutter, *Geol. Soc. Spec. Publ.*, 54, 71–79.
- Manighetti, I., G. C. P. King, Y. Gaudemer, C. H. Scholz, and C. Doubre (2001), Slip accumulation and lateral propagation of active normal faults in Afar, *J. Geophys. Res.*, 106, 13,667–13,696.
- Marrett, R., and R. W. Allmendinger (1991), Estimates of strain due to brittle faulting: Sampling of fault populations, *J. Struct. Geol.*, 13, 735–738.
- McKenzie, D. P., D. Davies, and P. Molnar (1970), Plate tectonics of the Red Sea and East Africa, *Nature*, 224, 125–133.
- Mohr, P. A., and B. Zanettin (1988), The Ethiopian flood basalt province, in *Continental Flood Basalts*, edited by J. D. Macdougall, pp. 63–110, Kluwer Acad., Dordrecht, Netherlands.
- Moore, J. M., and R. A. Schultz (1999), Processes of faulting in jointed rocks of Canyonlands National Park, Utah, *Geol. Soc. Am. Bull.*, 111, 808–822.
- Nicol, A., J. Watterson, J. J. Walsh, and C. Childs (1996), The shapes, major axis orientations and displacement patterns of fault surfaces, *J. Struct. Geol.*, 18, 235–248.
- Peacock, D. C. P. (2003), Scaling of transfer zones in British Isles, *J. Struct. Geol.*, 25, 1561–1567.
- Pickering, G., D. C. P. Peacock, D. J. Sanderson, and J. M. Bull (1997), Modeling tip zones to predict the throw and length characteristics of faults, *AAPG Bull.*, 81, 82–99.
- Pilger, A., and A. Rösler (1975), Afar depression of Ethiopia: International Symposium on the Afar Region and Related Rift Problems, *Sci. Rep.* 14, Int. Union Comm. on Geodyn., Bad Bergzabern, Germany.
- Polit, A. T., R. A. Schultz, and R. Soliva (2005), A tale of two stratigraphies: From Alba Patera to the Northern Plains, *Lunar Planet. Sci.*, XXXVI, abstract 2175.
- Poulimenos, G. (2000), Scaling properties of normal fault populations in the western Corinth Graben, Greece: Implications for fault growth in large strain settings, *J. Struct. Geol.*, 27, 307–322.
- Rives, T., M. Razack, J.-P. Petit, and K. Rawnsley (1992), Joint spacing: Analogue and numerical simulations, *J. Struct. Geol.*, 14, 925–937.
- Roeser, H. A. (1975), A detailed magnetic survey of the southern Red Sea, *Geol. Jahrb.*, 13, 131–153.
- Schlichte, R. W., S. S. Young, R. V. Ackermann, and A. Gupta (1996), Geometry and scaling relations of a population of very small rift-related normal faults, *Geology*, 24, 683–686.
- Scholz, C. H., and J. C. Contreras (1998), Mechanics of continental rift architecture, *Geology*, 26, 967–970.
- Scholz, C. H., and P. A. Cowie (1990), Determination of total strain from faulting using slip measurements, *Nature*, 346, 837–839.
- Scholz, C. H., N. H. Dawers, J.-Z. Yu, and M. H. Anders (1993), Fault growth and fault scaling laws: Preliminary results, *J. Geophys. Res.*, 98, 21,951–21,961.
- Schultz, R. A. (1999), Understanding the process of faulting: Selected challenges and opportunities at the edge of the 21st century, *J. Struct. Geol.*, 21, 985–993.
- Schultz, R. A. (2003), A method to relate initial elastic stress to fault population strains, *Geophys. Res. Lett.*, 30(11), 1593, doi:10.1029/2002GL016681.
- Schultz, R. A., and H. Fossen (2002), Displacement-length scaling in three dimensions: The importance of aspect ratio and application to deformation bands, *J. Struct. Geol.*, 24, 1389–1411.
- Schultz-Ela, D. D., and P. Walsh (2002), Modeling of grabens extending above evaporates in Canyon-

- lands National Park, Utah, *J. Struct. Geol.*, *24*, 247–275.
- Sigmundsson, F. (1992), Tectonic implications of the 1989 Afar earthquake sequence, *Geophys. Res. Lett.*, *19*, 877–880.
- Soliva, R. (2004), Croissance des failles normales dans les séries stratifiées hétérogènes: Rôle de la restriction verticale et de la coalescence sur les lois d'échelles et la distribution spatiale des failles, Exemples naturels et approche théorique, Ph.D. thesis, Univ. Paris-Sud XI, Orsay.
- Soliva, R., and A. Benedicto (2004), A linkage criterion for segmented normal faults, *J. Struct. Geol.*, *26*, 2251–2267.
- Soliva, R., and A. Benedicto (2005), Geometry, scaling relation and spacing of vertically restricted normal faults, *J. Struct. Geol.*, *27*, 317–325.
- Soliva, R., R. A. Schultz, and A. Benedicto (2005), Three-dimensional displacement-length scaling and maximum dimension of normal faults in layered rocks, *Geophys. Res. Lett.*, *32*, L16302, doi:10.1029/2005GL023007.
- Soliva, R., A. Benedicto, and L. Maerten (2006), Spacing and linkage of confined normal faults: Importance of mechanical thickness, *J. Geophys. Res.*, *111*, B01402, doi:10.1029/2004JB003507.
- Sornette, A., P. Davy, and D. Sornette (1990), Growth of fractal fault patterns, *Phys. Rev. Lett.*, *65*, 2266.
- Spyropoulos, C., W. J. Griffith, C. H. Scholz, and B. E. Shaw (1999), Experimental evidence for different strain regimes of crack populations in a clay model, *Geophys. Res. Lett.*, *26*, 1081–1084.
- Taieb, M. (1975), Evolution of Plio/Pleistocene sedimentary basin of the central Afar (Awash Valley, Ethiopia), in *Afar Depression of Ethiopia*, edited by A. Pigler and A. Rosler, pp. 80–87, E. Schweizerbart'sche, Stuttgart, Germany.
- Tapponier, P., R. Armijo, I. Manighetti, and V. Courtillot (1990), Bookshelf faulting and horizontal block rotations between overlapping rift zones in southern Afar, *Geophys. Res. Lett.*, *17*, 1–4.
- Trudgill, B., and J. Cartwright (1994), Relay ramp forms and normal-fault linkages, Canyonlands National Park, Utah, *Geol. Soc. Am. Bull.*, *106*, 1143–1157.
- Varet, J., and F. Gasse (1978), Geology of central and southern Afar (Ethiopia and Djibouti Republic), report, Cent. Natl. de la Rech. Sci., Paris.
- Villemin, T., and C. Sunwoo (1987), Distribution logarithmique self similaire des rejets et longueurs de failles: Exemple du bassin Houiller Lorrain, *C. R. Acad. Sci., Ser. II*, *305*, 1309–1312.
- Walsh, J. J., and J. Watterson (1987), Distribution of cumulative displacement and seismic slip on a single normal fault surface, *J. Struct. Geol.*, *9*, 1039–1046.
- Walsh, J. J., J. Watterson, and G. Yielding (1991), The importance of small-scale faulting in regional extension, *Nature*, *351*, 391–393.
- Walsh, J. J., W. R. Bailey, C. Childs, A. Nicol, and C. G. Bonson (2003), Formation of segmented normal faults: A 3-D perspective, *J. Struct. Geol.*, *26*, 399–400.
- Wilkins, S. J., and M. R. Gross (2002), Normal fault growth in layered rocks at split mountain, Utah: Influence of mechanical stratigraphy on dip linkage, fault restriction and fault scaling, *J. Struct. Geol.*, *24*, 1413–1429.
- Willemsse, E. J. M. (1997), Segmented normal faults: Correspondence between three-dimensional mechanical models and field data, *J. Geophys. Res.*, *102*, 675–692.
- WoldeGabriel, G., J. L. Aronson, and R. C. Walter (1990), Geology, geochronology, and rift basin development in the central sector of the Main Ethiopian rift, *Geol. Soc. Am. Bull.*, *102*, 439–485.
- Wolfenden, E., C. Ebinger, D. Yirgu, A. Deino, and D. Ayalew (2004), Evolution of the northern Main Ethiopian rift: Birth of a triple junction, *Earth Planet. Sci. Lett.*, *224*, 213–228.
- Zanentini, B., and E. Juste-Visentin (1975), Tectonical and volcanological evolution of the western Afar margin (Ethiopia), in *Afar Depression of Ethiopia*, edited by A. Pigler and A. Rosler, pp. 38–54, E. Schweizerbart'sche, Stuttgart, Germany.

---

R. A. Schultz, Geomechanics–Rock Fracture Group, Department of Geological Sciences and Engineering, University of Nevada, Reno, NV 89557–0138, USA. (schultz@mines.unr.edu)

R. Soliva, Laboratoire Géosciences Montpellier, Université Montpellier II, F-34000 Montpellier, France. (roger.soliva@dstu.univ-montp2.fr)